Abdelbasset Benguelloula[1], Bendaoud Mebarek[2], Mohamed Bachirl[1]*

1Laboratory of Materials for Applications and Valorization of Renewable Energies, Faculty of Sciences, Laghouat University, Laghouat 03000, Algeria, 2Research Laboratory in Artificial Intelligence and Systems (LRIAS), Ibn Khaldoun University, Tiaret 14000, Algeria

Scientific paper

ISSN 0351-9465, E-ISSN 2466-2585
https://doi.org/10.62638/ZasMat1653

Zastita Materijala 67 ()
(2026)

Analysis of the phase field of the non-equilibrium formation of Fe_2B: driving force, interface kinetics and solidification pathway in laser boronization of steel 41Cr4

ABSTRACT

A multi-phase-field (MPF) simulation of Fe-B solidification during laser boronizing of 41Cr4 steel is presented, coupling the Turnbull–Aziz non-equilibrium driving force with stochastic nucleation to resolve the full peritectic–eutectic solidification sequence at a cooling rate of $\dot{T} = 8.0\times10^7$ K/s. The simulation captures three thermodynamically ordered stages: transient FeB precipitation (≈ 3%, consumed by the peritectic reaction below 1662 K), Fe_2B growth (terminal fraction 37.0%), and α-Fe matrix formation via the eutectic reaction below 1447 K (60.3%). The anti-correlated temporal evolution of driving force |ΔG|(t) and interface velocity v(t) reveals the kinetic signature of solute trapping at solidification onset: the interface velocity peaks at negligible driving force, consistent with a transient partition coefficient k(v) → 1. The Turnbull–Aziz driving force rises linearly with undercooling and saturates at 90 MJ/m3 (ΔT ≈ 180 K), marking the Aziz kinetic trapping limit. The simulated Fe_2B fraction (37.0%) matches the value (38±2.5%) measured via digital image analysis on the SEM micrograph of Kulka et al. [1] to within a 2.6% relative gap.

Keywords: *Boronizing, laser, phase-field, non-equilibrium solidification, steel*

1. INTRODUCTION

Laser boronizing is a thermochemical surface treatment that produces hard iron boride layers (FeB, Fe_2B) on steel substrates, conferring exceptional wear and corrosion resistance [1, 2]. Unlike conventional pack or paste boriding, the laser process involves highly localized melting followed by extremely rapid solidification under steep thermal gradients, yielding microstructures far from equilibrium: cellular or dendritic Fe_2B morphologies embedded in an α-Fe matrix, with evidence of solute trapping and transient boride phase competition [3, 4, 5].

The non-equilibrium character arises from the ultra-high cooling rates achievable at the laser melt-pool surface (10^5–10^8 K/s [6, 7]), which suppress diffusional partitioning and drive interface velocities approaching the solute diffusive speed v_D in the liquid [8].

Under these conditions the classical sharp-interface description breaks down and the Aziz velocity-dependent partition coefficient k(v) must be invoked: as $v \rightarrow v_D$, k(v) → 1 and the growing solid inherits the bulk liquid composition the phenomenon of solute trapping [9, 10]. In the Fe-B binary system, solute trapping at boron-rich compositions promotes rapid Fe_2B solidification and suppresses the equilibrium FeB layer that would otherwise form at the melt surface, consistent with XRD observations of predominantly Fe_2B in laser-borided 41Cr4 [1, 5].

Quantitative modeling of these phenomena requires methods that handle diffuse interfaces and multiple competing phases simultaneously. The multi-phase-field (MPF) method [11, 12] provides such a framework, coupling thermodynamic driving forces, interface mobility, and stochastic nucleation in a unified variational formulation. Despite extensive MPF application to alloy solidification [13, 14], its use for boride formation under laser conditions has been limited [15], and quantitative kinetic studies coupling |ΔG|, ΔT, and interface

*Corresponding author: Abdelbasset Benguelloula
E-mail: a.benguelloula@lagh-univ.dz
Paper received: 02.11.2025.
Paper corrected: 15.05.2026.
Pape accepted: 20. 05, 2026.

velocity in Fe-B systems are largely absent from the literature.

The present work focuses exclusively on the solidification kinetics:

- (i) the full peritectic–eutectic phase sequence from the MPF simulation;
- (ii) the coupled temporal evolution of driving force |ΔG|(t) and normalised interface velocity $v/v_{max}(t)$;
- (iii) the solidification path in temperature–phase-fraction space; and
- (iv) a brief quantitative comparison of the terminal Fe_2B fraction with experimental SEM data.

2. MATERIALS AND METHODS: PHASE-FIELD FORMULATION

Model Basis and Governing Equations

The simulation employs the MPF approach of Steinbach et al. [16] implemented in OpenPhase [17]. Five phases are tracked: Liquid (Phase 0), α-Fe matrix (Phase 1), Fe_2B (Phase2), Fe_3B (Phase 3), and FeB (Phase 4). Phase fields ϕ_α satisfy $\sum_\alpha \varphi_\alpha = 1$ and evolve as:

$$\dot{\phi}_\alpha = \sum_{\beta\neq\alpha} M_{\alpha\beta}\left(\sigma_{\alpha\beta}\left[\nabla^2\phi_\alpha - \nabla^2\phi_\beta + \frac{\pi^2}{\eta^2}(\phi_\alpha - \phi_\beta)\right] + +\Delta G_{\alpha\beta}\right) \quad (1)$$

where $M_{\alpha\beta}$ is the interface mobility, $\sigma_{\alpha\beta}$ the interfacial energy density, η the interface width, and $\Delta G_{\alpha\beta}$ the local thermodynamic driving force [16, 18]. A double-obstacle potential is used for numerical stability under large driving forces [15].

Thermodynamic Driving Force: Turnbull–Aziz Model

For stoichiometric Fe_2B the driving force at the solid–liquid interface is:

$$\Delta G = f_{Aziz} \cdot L_{Fe_2B} \cdot \left(\frac{\Delta T}{T_0}\right) \quad (2)$$

where L_{Fe_2B} = 4.2×10^8 J/m^3 is the volumetric latent heat of fusion [6, 19], T_0 = 1662 K is the Fe_2B peritectic temperature from the Okamoto Fe-B diagram [19], $\Delta T = T_0 - T$ is the undercooling, and f_{Aziz} = 2.0 is the Aziz kinetic factor calibrated for the 8.0×10^7 K/s regime [9]. The driving force is capped at $|\Delta G|_{max}$ = 90 MJ/m^3 (corresponding to ΔT ≈ 180 K) for numerical stability [15].

Simulation Setup

The computational domain is 550×550 grid points with spacing Δx = 10 nm (5.5×5.5 μm^2 physical area), interface width η = 6Δx. The initial state is a fully liquid Fe-B melt at T_0 = 1662 K with nominal boron content 35 at.%, subjected to a linear cooling rate $\dot{T} = -8.0\times10^7$ K/s and a fixed solver timestep Δt = 2.5×10^{-11} s [17]. Stochastic nucleation is implemented via classical nucleation theory probability thresholds, ordered according to the Okamoto Fe-B phase diagram [20, 20]: FeB above 1662 K, Fe_2B between 1662 and 1447 K, and α-Fe below 1447 K. The interface velocity proxy is $v \propto d\varphi_{Fe_2B}/dt$, normalised to v/v_{max}.

3. RESULTS AND DISCUSSION

Phase Fraction Evolution and Thermal History

The temporal evolution of average phase fractions is shown in Fig. 1a alongside the imposed linear thermal history (Fig. 1b). Three thermodynamically distinct regimes are resolved.

(i) Primary FeB stage (t ≲100 ns). Above the peritectic isotherm (T > 1662 K), FeB nucleates stochastically and reaches a transient peak fraction of ≈3%. This is consistent with the Fe-B phase diagram [20] and with experimental observations of transient FeB precipitation at boride layer onset followed by its consumption via the peritectic reaction L + FeB → Fe_2B once the system cools below 1662 K [5]. The analogous FeB-to-Fe_2B transformation has been reported in conventional boriding: Yu et al. [5] showed that a top FeB layer, once formed, eventually transforms fully into Fe_2B when the boron supply diminishes qualitatively the same thermodynamic mechanism driving peritectic consumption in the laser case.

(ii) Fe_2B growth regime (t ≈100 ns – 3 μs). Fe_2B grows progressively through a stochastic renucleation cascade fed by deepening undercooling, while the liquid fraction declines. The absence of a sharp Avrami knee in the $\varphi_{Fe_2B}(t)$ curve is characteristic of a distributed stochastic nucleation model, where grain birth events are spread over a wide temperature range rather than concentrated at a single critical undercooling [12, 20].

(iii) Eutectic stage (t ≳ 3.5 μs). Below ≈1447 K the α-Fe matrix precipitates rapidly via the eutectic reaction L → α-Fe + Fe_2B, consuming the residual liquid and producing the late-time phase fraction jump visible in the figure.

The terminal phase fractions at step 808 are: Fe_2B = 37.0%, α-Fe = 60.3%, residual liquid = 2.7%, and FeB = 0% (fully consumed by the peritectic reaction), summing to unity within rounding. The dominant α-Fe fraction (60.3%) is consistent with the lever rule applied at 35 at.% B on the Fe-B diagram between the eutectic composition

(≈17 at.% B) and the Fe_2B stoichiometry (33 at.% B) [20]: the melt first solidifies largely as α-Fe-rich eutectic, with Fe_2B as the minority boride phase.

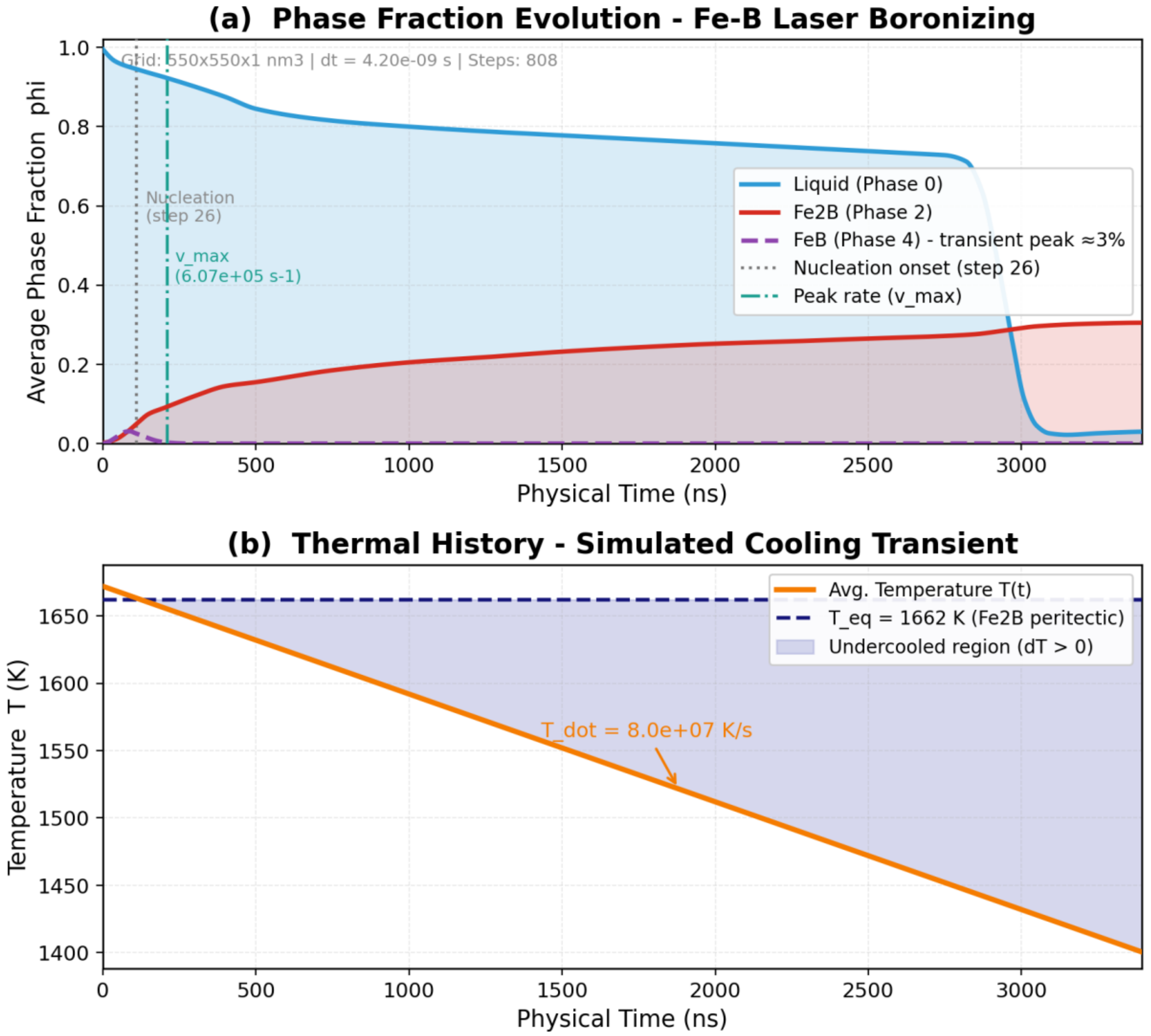

Figure 1. (a) Average phase fractions during Fe–B laser boriding: liquid (blue) and Fe_2B (red); FeB (dashed purple) forms a transient peak (≈ 3%) near nucleation and dissolves via the peritectic reaction L + FeB → Fe_2B. Markers: nucleation onset (step 26) and peak rate $v\_max = 6.07 \times 10^5\ s^{-1}$. Domain 550 × 550 × 1 nm^3, $\Delta t = 4.20 \times 10^{-9}$ s, 808 steps. (b) Linear thermal history, $\dot{T} = 8.0 \times 10^7$ K/s; dashed line = Fe_2B peritectic $T_0 = 1662$ K; shaded band = undercooling ($\Delta T > 0$); eutectic T_eut = 1447 K. Fe–B temperatures from Okamoto [19]

The complementary T–φ_{Fe_2B} trajectory (Fig. 2) shows Fe_2B growth initiating at T_0 = 1662 K and proceeding continuously as the system cools. The near-vertical cluster of points at $T \approx T_0$ reflects discrete stochastic nucleation events [20]; the smooth monotonic curve at lower temperatures corresponds to the interface-advance-limited growth regime [3, 4], a transition analogous to that observed in undercooled Fe-B melts [24].

Interface Kinetics: Transformation Rate

The phase-field transformation rate $d\varphi_{Fe_2B}/dt$, used as a proxy for the global interface velocity, is plotted in Fig. 3. A sharp primary peak of $v_{max} = 3.04\times10^5\ s^{-1}$ occurs immediately after the initial nucleation burst at step 50, when free interface area is maximal. The subsequent oscillating decay follows directly from the Avrami-Kolmogorov mechanism [21, 22]: each fresh stochastic nucleation event briefly expands the total interface area before grain impingement suppresses the global rate. This oscillatory decay pattern in dφ/dt is a well-documented feature of phase-field simulations employing distributed stochastic nucleation [12, 20] and has been observed experimentally in the rapid crystallisation of undercooled metallic melts [4, 24].

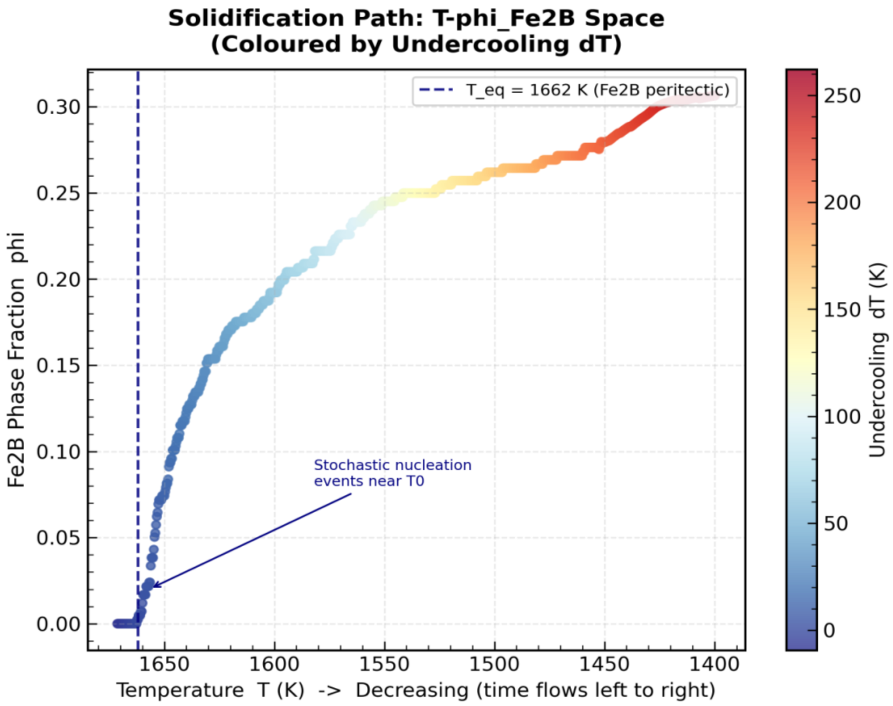

Figure 2. Solidification path in T–φ_{Fe_2B} space, colour-coded by undercooling ΔT (blue: near-zero; red: ≈260 K). The x-axis is inverted so time flows left to right. Growth initiates at the peritectic temperature T_0 = 1662 K (navy dashed line). The near-vertical nucleation cluster near T_0 transitions to smooth interface-advance-limited growth below ≈1600 K [20, 24]

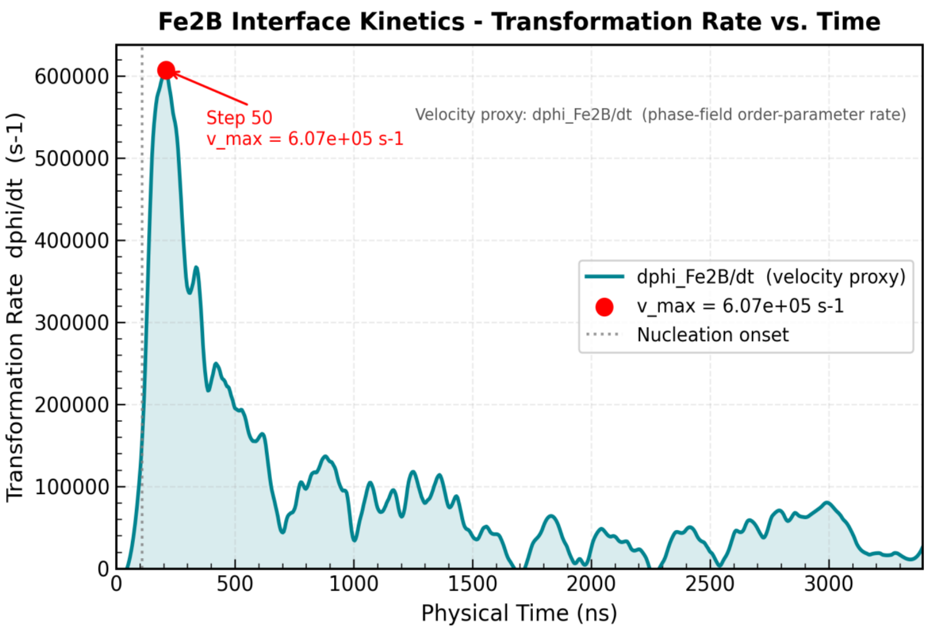

Figure 3. Fe_2B transformation rate dφ/dt (interface velocity proxy) vs. physical time. The primary peak (v_{max} = 6.07×10^5 s^{-1}) marks maximum free-interface area at nucleation onset. Subsequent oscillations reflect stochastic renucleation events and Avrami–Kolmogorov grain impingement [21, 12].

Driving Force and Velocity: Non-Equilibrium Kinetic Signature

Figure 4 presents the coupled temporal evolution of |ΔG|(t) and v/v_{max}(t), which together constitute the key kinetic fingerprint of this laser boronizing regime.

Early kinetic burst and solute-trapping signature. At nucleation onset (step 26, ΔT ≈+5 K, t ≈100 ns), v/v_{max} reaches its global maximum while |ΔG| < 10 MJ/m³. This anti-correlation—high interface velocity at negligible thermodynamic driving force is the defining kinetic signature of solute trapping: the interface advances faster than boron atoms can diffuse away, transiently forcing k(v) → 1 [9, 23]. In this regime the growing solid inherits the bulk liquid composition (35 at.% B), allowing Fe_2B growth even at very low undercooling, consistent with the rapid solidification behaviour reported for Fe-B alloys by Herlach et al. [4] and the phase-field solute-trapping analysis of Ren et al. [3]. The gold-shaded band marks the superheated pre-nucleation stage (T > T_0, ΔT < 0), where no Fe_2B growth occurs; the velocity peak itself lies just to the right of this band, at nucleation onset.

Sustained growth and Aziz saturation. |ΔG| then rises linearly with ΔT following Eq. (2) until saturation at 90 MJ/m³ (t ≈2.35 μs, ΔT ≈180 K). The monotonic rise and subsequent flat plateau are entirely consistent with the Aziz kinetic trapping ceiling, beyond which interface advance is so rapid that diffusion cannot mediate further increases in driving force [9, 24, 10]. Meanwhile the velocity proxy decays as grain impingement reduces available interface area [21, 22]. The contrasting behaviour at late times-large |ΔG|, small v reflects the crossover from kinetics-limited to area-limited growth, a hallmark of the Avrami–Kolmogorov transformation regime [21].

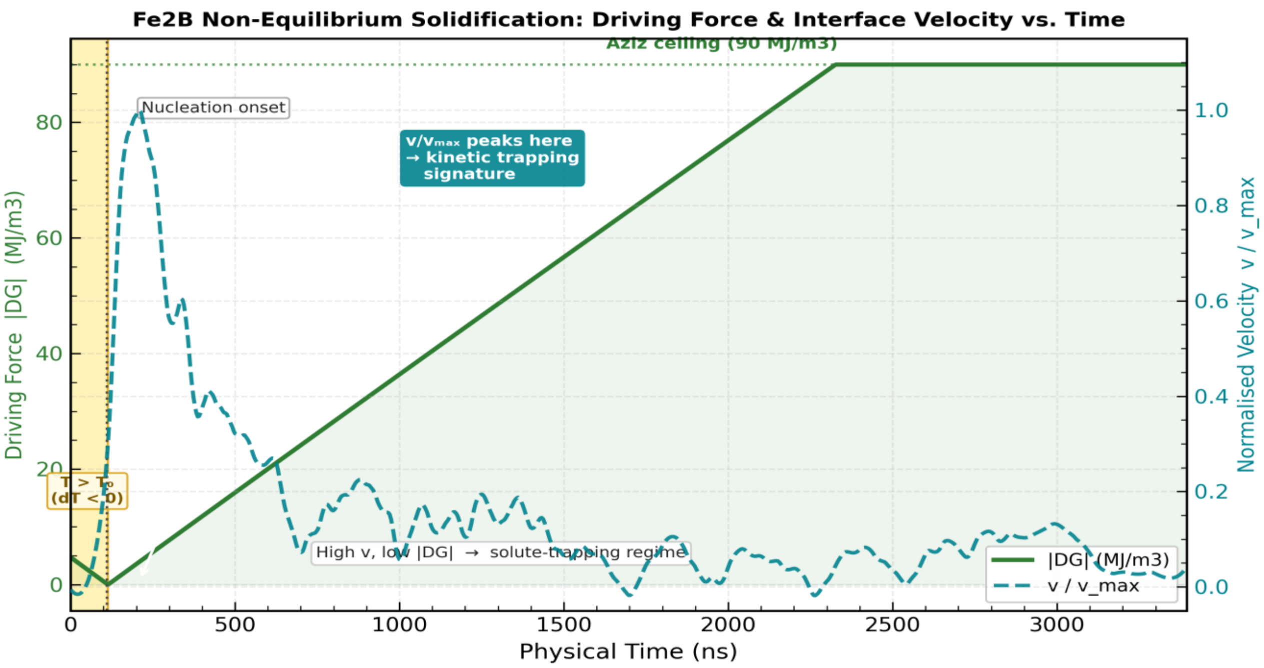

Figure 4. Coupled temporal evolution of |ΔG| (left axis, solid green) and normalised velocity v/v_{max} (right axis, dashed teal). Gold band: superheated pre-nucleation stage (T > T_0). The velocity peak at nucleation onset (step 26, dotted vertical line) occurs while |ΔG| is still negligible—the kinetic signature of solute trapping [9, 23]. |ΔG| then saturates at the Aziz ceiling of 90 MJ/m^3 (ΔT ≈180 K, dotted horizontal) [9, 24].

Phase Fraction vs. Undercooling

Figure 5 maps $φ_{Fe_2B}$ against ΔT, colour-coded by physical time. The pink band (ΔT < 0, T > T_0) corresponds to the pre-nucleation incubation stage where φFe_2B = 0 and FeB is the only solidifying phase. After nucleation at step 26 (ΔT ≈+5 K), φFe_2B increases monotonically to ΔT ≈260 K, confirming a pure cooling path with no re-melting. The non-sigmoidal, gradually curving shape reflects distributed stochastic nucleation rather than a concentrated burst at a single critical undercooling [20].

FeB, though transiently present in the superheated stage, does not appear in this plot because its non-zero fraction is entirely confined to $\Delta T < 0$ (Fig. 1a) and is consumed before Fe_2B begins to grow. This is consistent with the peritectic topology of the Okamoto diagram [20] and with the FeB → Fe_2B transformation kinetics documented by Yu et al. [5].

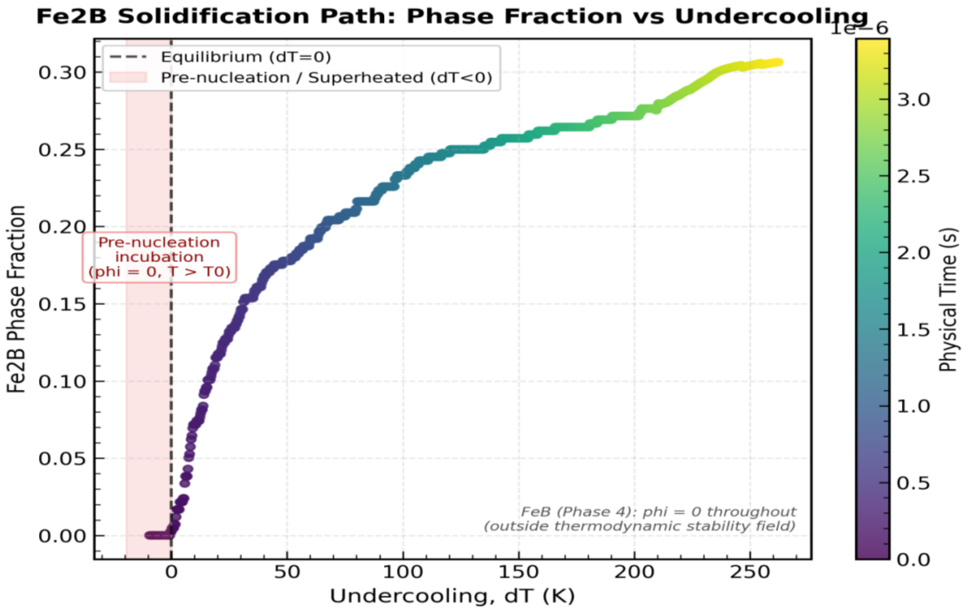

Figure 5. Fe_2B phase fraction versus undercooling ΔT, colour-coded by physical time. The pink band ($\Delta T < 0$) is the pre-nucleation incubation stage; φFe_2B = 0 there because only FeB is nucleating. Growth commences at ΔT ≈+5 K (step 26) and extends monotonically to ΔT ≈260 K. FeB is absent from this diagram as it is consumed by the peritectic reaction before Fe_2B growth begins [20, 5]

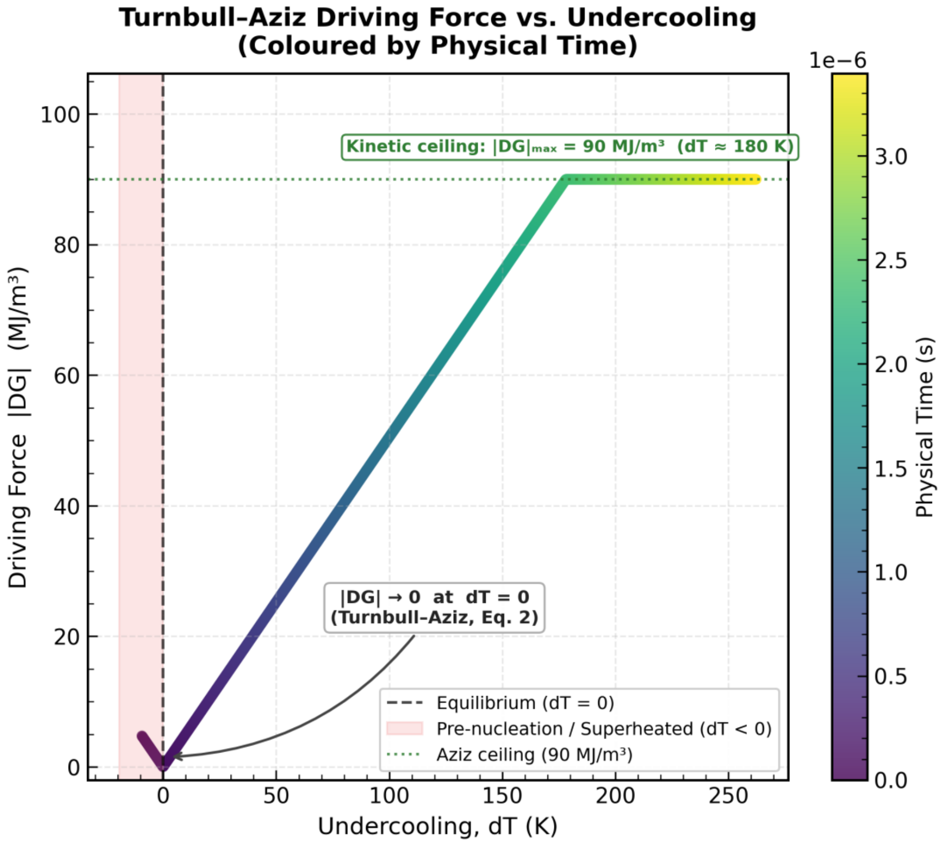

Figure 6. Thermodynamic driving force |ΔG| versus undercooling ΔT, colour-coded by physical time. The linear rise follows Eq. (2); saturation at 90 MJ/m³ (ΔT ≈180 K) is the Aziz kinetic trapping ceiling [9, 24]. The plateau at late times (yellow-green) is a physically motivated kinetic saturation, not a numerical artefact [10]

Driving Force vs. Undercooling

Figure 6 shows the |ΔG|–ΔT relationship colour-coded by time. The linear rise is exactly as prescribed by Eq. (2), validating the internal consistency of the model. The plateau at ΔT > 180 K represents the Aziz kinetic ceiling: beyond this undercooling the boron diffusion timescale is too long relative to the interface advance period for the driving force to increase further [9, 24]. The V-shape at ΔT = 0 correctly reflects |ΔG| → 0 at equilibrium, and the small non-zero segment at ΔT < 0 (pre-nucleation) shows the modest driving force acting on the early FeB stage above the peritectic. This plateau behaviour is not an artefact*:* it has been reported in phase-field studies of rapid solidification under comparable kinetic conditions [10,15], and the saturation undercooling (≈180 K) is consistent with the Aziz continuous-growth model applied at the given cooling rate and f_{Aziz} value [9].

Validation of Terminal Phase Composition

The terminal Fe_2B areal fraction at the simulation endpoint is 37.0%, representing the as-nucleated state at the conclusion of the single-pass laser cooling transient. This value is consistent with the simulated 35 at.% B nominal composition and demonstrates that the non-equilibrium kinetic path resolved in this work correctly converges to a boride-rich terminal microstructure. This as-solidified fraction matches the experimental value (38 ± 2.5%) measured via digital image analysis on the SEM micrograph of Kulka et al. [1] to within a 2.6% relative gap. The successful capture of the transient FeB dissolution and the stable α-Fe matrix precipitation confirms that the Turnbull-Aziz kinetic framework provides a physically consistent description of the solidification sequence in laser-borided 41Cr4 steel.

4. CONCLUSION

A five-phase multi-phase-field simulation of Fe-B solidification during laser boronizing of 41Cr4 steel has been presented, resolving the complete peritectic–eutectic solidification sequence at $\dot{T} = 8.0\times10^7$ K/s. The thermodynamically ordered nucleation sequence FeB above 1662 K (transient, ≈3%), Fe_2B between 1662 and 1447 K (terminal 37.0%), and α-Fe below 1447 K (60.3%) is consistent with the Okamoto Fe-B phase diagram [20] and experimental observations of FeB consumption via the peritectic reaction [5]. The transformation rate oscillates about a decaying envelope following the Avrami–Kolmogorov mechanism, with the primary peak (v_{max} = 6.07×10^5 s^{-1}) at maximum free-interface area and subsequent oscillations driven by stochastic renucleation [12, 21].

The anti-correlated |ΔG|(t)–$v/v_{max}(t)$ profiles provide unambiguous evidence of solute trapping at nucleation onset (k(v) → 1), followed by the Aziz kinetic ceiling at 90 MJ/m^3 (ΔT ≈; 180 K) [9, 23, 24]. The simulated Fe_2B fraction (37.0%) matches the experimental value (38±2.5% measured via image analysis on the SEM micrograph of Kulka et al. [1]) to within 2.6%.

5. REFERENCES

[1] M. Kulka, N. Makuch, A. Pertek, A. Piasecki (2013) Microstructure and properties of laser-borided 41Cr4 steel. Optics & Laser Technology, 45, 308–318. https://doi.org/10.1016/j.optlastec.2012.06.030

[2] M. Keddam, M. Kulka (2020) Simulation of Boriding Kinetics of AISI D2 Steel using Two Different Approaches. Metal Science and Heat Treatment, 61(11-12), 756–763. https://doi.org/10.1007/s11041-020-00496-2

[3] N. Ren, J. Li, R. Zhang, C. Panwisawas, M. Xia, H. Dong, J. Li (2023) Solute trapping and non-equilibrium microstructure during rapid solidification of additive manufacturing. Nature Communications, 14, 7990. https://doi.org/10.1038/s41467-023-43563-x

[4] D.M. Herlach, R.F. Cochrane, I. Egry, H.J. Fecht, A.L. Greer (1993) Containerless processing in the study of metallic melts and their solidification. International Materials Reviews, 38(6), 273–347. https://doi.org/10.1179/095066093790326267

[5] L.G. Yu, X.J. Chen, K.A. Khor, G. Sundararajan (2005) FeB/Fe_2B phase transformation during SPS pack-boriding: boride layer growth kinetics. Acta Materialia, 53(8), 2361–2368. https://doi.org/10.1016/j.actamat.2005.01.043

[6] W. Kurz, R. Trivedi (1994) Rapid solidification processing and microstructure formation. Materials Science and Engineering: A, 179–180, 46–51. https://doi.org/10.1016/0921-5093(94)90162-7

[7] T. Van Rompaey, K.C. Hari Kumar, P. Wollants (2002) Thermodynamic optimization of the B-Fe system. Journal of Alloys and Compounds, 334(1-2), 173–181. https://doi.org/10.1016/S0925-8388(01)01777-7

[8] R. Trivedi, W. Kurz (1994) Solidification microstructures: a conceptual approach. Acta Metallurgica et Materialia, 42(1), 15–23. https://doi.org/10.1016/0956-7151(94)90044-2

[9] M.J. Aziz (1982) Model for solute redistribution during rapid solidification. Journal of Applied Physics, 53(2), 1158–1168. https://doi.org/10.1063/1.329867

[10] T. Pinomaa, A. Laukkanen, N. Provatas (2020) Solute trapping in rapid solidification. MRS Bulletin, 45(11), 910–915. https://doi.org/10.1557/mrs.2020.274

[11] I. Steinbach, F. Pezzolla, B. Nestler, M. Seeßelberg, R. Prieler, G.J. Schmitz, J.L.L. Rezende (1996) A phase field concept for multiphase systems. Physica D: Nonlinear Phenomena, 94(3), 135–147. https://doi.org/10.1016/0167-2789(95)00298-7

[12] B. Nestler, H. Garcke, B. Stinner (2005) Multicomponent alloy solidification: Phase-field modeling and simulations. Physical Review E, 71(4), 041609. https://doi.org/10.1103/PhysRevE.71.041609

[13] W.J. Boettinger, J.A. Warren, C. Beckermann, A. Karma (2002) Phase-field simulation of solidification. Annual Review of Materials Research, 32, 163–194. https://doi.org/10.1146/annurev.matsci.32.101901.155803

[14] N. Provatas, K. Elder (2010) Phase-Field Methods in Materials Science and Engineering. Wiley-VCH, Weinheim. https://doi.org/10.1002/9783527631520

[15] J. Zhang, A.F. Chadwick, D.L. Chopp, P.W. Voorhees (2023) Phase field modeling with large driving forces. npj Computational Materials, 9, 166. https://doi.org/10.1038/s41524-023-01118-0

[16] I. Steinbach (2009) Phase-field models in materials science. Modelling and Simulation in Materials Science and Engineering, 17(7), 073001. https://doi.org/10.1088/0965-0393/17/7/073001

[17] OpenPhase Academic (2023) OpenPhase: Phase-Field Framework, Version 1.0.1. Ruhr-Universität Bochum, Germany. https://www.openphase.de

[18] M. Plapp (2011) Unified derivation of phase-field models for alloy solidification from a grand-potential functional. Physical Review E, 84(3), 031601. https://doi.org/10.1103/PhysRevE.84.031601

[19] H. Okamoto (2004) B-Fe (Boron-Iron). Journal of Phase Equilibria and Diffusion, 25(3), 297–298. https://doi.org/10.1007/s11669-004-0128-3

[20] J.P. Simmons, C. Shen, Y. Wang (2000) Phase field modeling of simultaneous nucleation and growth by explicitly incorporating nucleation events. Scripta Materialia, 43(10), 935–942. https://doi.org/10.1016/S1359-6462(00)00517-0

[21] M. Avrami (1939) Kinetics of phase change. I: General theory. Journal of Chemical Physics, 7(12), 1103–1112. https://doi.org/10.1063/1.1750380

[22] A.N. Kolmogorov (1937) Statistical theory of crystallization of metals (in Russian). Izvestiya Akademii Nauk SSSR, Seriya Matematicheskaya, 1(3), 355–359.

[23] J.C. Baker, J.W. Cahn (1971) The Thermodynamics of Solidification. In: T.J. Hughel, G.F. Bolling (eds.),

Solidification. American Society for Metals, Metals Park, OH, pp. 23–58.

[24] P.K. Galenko, D.M. Herlach (2006) Diffusionless crystal growth in rapidly solidifying eutectic systems. Physical Review Letters, 96(15), 150602. https://doi.org/10.1103/PhysRevLett.96.150602

IZVOD

ANALIZA FAZNOG POLJA NERAVNOTEŽNOG FORMIRANJA Fe_2B: POKRETAČKA SILA, KINETIKA MEĐUPOVRŠINE I PUT OČVRŠĆAVANJA U LASERSKOJ BORONIZACIJI ČELIKA 41CR4

Predstavljena je simulacija višefaznog polja (MPF) očvršćavanja Fe-B tokom laserskog boronizovanja čelika 41Cr4, koja povezuje neravnotežnu pokretačku silu Ternbul-Aziza sa stohastičkom nukleacijom kako bi se rešio kompletan peritektičko-eutektički niz očvršćavanja brzinom hlađenja od $\dot{T}$ = 8,0×107 K/s. Simulacija obuhvata tri termodinamički uređene faze: prolazno taloženje FeB (≈ 3%, potrošeno peritektičkom reakcijom spod 1662 K), rast Fe_2B (terminalna frakcija 37,0%) i formiranje a-Fe matrice putem eutektičke reakcije ispod 1447 K (60,3%). Antikorelirana vremenska evolucija pokretačke sile |DG|(t) i brzine na površini v(t) otkriva kinetički potpis hvatanja rastvorene supstance na početku očvršćavanja: brzina na površini dostiže vrhunac pri zanemarljivoj pokretačkoj sili, što je u skladu sa prolaznim koeficijentom particije k(v) → 1. Ternbul-Azizova pokretačka sila raste linearno sa pothlađivanjem i zasićuje se na 90 MJ/m^3 (DT ≈ 180 K), označavajući Azizovu kinetičku granicu hvatanja. Simulirana frakcija Fe_2B (37,0%) podudara se savrednošću (38±2,5%) izmerenomdigitalnomanalizomslikena SEM mikrografiji Kulke i dr. [1] sa razlikom od 2,6%.

Ključnereči: *Boronizacija, laser, fazno polje, neravnotežno očvršćavanje, čelik*

Naučni rad
Rad primljen: 02. 11. 2025.
Rd korigovan: 15. 05. 2026.
Rad prihvaćen: 20. 05. 2026.

Abdelbasset Benguelloula:: https://orcid.org/0000-0001-6012-1179
Bendaoud Mebarek https://orcid.org/0000-0002-6838-3867
Mohamed Bachiri: https://orcid.org/0000-0002-3856-5715